

# Amplitude and Wavelength Effects for Wavy Channels

**Thomas M. Corbett<sup>1</sup>**

Department of Mechanical Engineering,  
Pennsylvania State University,  
State College, PA 16801  
e-mail: tmc5980@psu.edu

**Karen A. Thole**

Department of Mechanical Engineering,  
Pennsylvania State University,  
State College, PA 16801  
e-mail: kthole@psu.edu

**Sudhakar Bollapragada**

Solar Turbines Incorporated,  
San Diego, CA 92101  
e-mail: bollapragada\_sudhakar@  
solar-turbines.com

*To improve the efficiency and durability of gas turbine components, advancements are needed in cooling technologies. To accomplish this task, some manufacturers are turning to additive manufacturing (AM), as it offers the ability to both rapidly iterate on component design as well as incorporate unique internal cooling structures directly into parts. As one example, wavy microchannels can be readily integrated into turbine components. This study investigates wavy channels of varying channel amplitude and wavelength through experimental measurements of heat transfer and pressure loss. In addition to experimental testing, computational fluid dynamics (CFD) predictions were made to identify internal flow features that impacted performance. Five channel geometries were integrated into test coupons that were additively manufactured out of Hastelloy-X using direct metal laser sintering. True coupon geometric characteristics and wall roughness values were captured non-destructively using computed tomography (CT) scans. Geometric analyses indicated that coupons were reproduced accurately with minimal deviation from design intent. Experimental results indicated that decreasing the channel wavelength and increasing the channel amplitude resulted in substantial increases in both bulk friction factor and Nusselt number with respect to the nominal case and were scaled using a relative waviness parameter. CFD simulations predicted significant mixing of flow in the cases with the smallest wavelength and greatest amplitude. [DOI: 10.1115/1.4055612]*

**Keywords:** computational fluid dynamics (CFD), heat transfer and film cooling

## Introduction

The efficiency of gas turbine engines is important for many reasons, especially given the impacts on the economy and environment. Airlines use approximately 20% of all revenue on fuel alone (depending upon the market) [1] and the burning of CO<sub>2</sub> producing fossil fuels is directly related to the increasing rate of climate change. To address these issues, it is common practice to improve the engine efficiency by raising the operating temperature of the turbine. This process requires increasingly innovative methods to cool both rotating and static turbine components while minimizing the use of cooling air. Traditionally, many types of cooling technologies, such as microchannels, pin fins, ribs, and more, have been integrated into turbine components, and each have been explored at length [2].

One such internal cooling technology, wavy channels, is of particular interest. It is possible for wavy channels to be integrated into many static turbine parts, such as the blade outer air seal or shrouds, in combustor liners, or in turbine airfoils as a potential concept in considering double-wall cooling designs that are often used. Turbine manufacturers have already demonstrated the use of this concept in actual turbine components [3]. Wavy microchannels have been explored for several decades in many low Reynolds number studies; however, their implementation and use in conjunction with additive manufacturing (AM) have only recently begun to be studied for turbine applications.

To facilitate these developments and construct complex parts, some manufacturers are turning to additive manufacturing. AM offers many benefits over traditional methods, such as increased part complexity without significant increase in cost, the ability to imbed novel internal features that would have been otherwise impossible, and the capacity to quickly iterate on designs. One of the primary AM methods of pertinence for gas turbines is direct metal laser sintering (DMLS) due to its ability to produce fine

details and growing material selection. While there are elements of AM design that are unique to the process and require further consideration, such as build angle and process parameters, understanding and taking advantage of these barriers can make AM a highly effective tool for developing components with advanced cooling schemes.

This study expands on prior wavy channels studies by investigating how the amplitude and wavelength independently impact the pressure loss and heat transfer of AM wavy microchannels. To characterize these effects, five AM test coupons were printed using DMLS and then tested to capture their heat transfer and pressure loss performance. These results were explored further through computational fluid dynamics (CFD) analysis which identified the internal flow features that facilitate or hamper performance.

## Literature Review

Wavy channels are beneficial to cooling performance due to their ability to generate unique flow structures not present in straight channels. Many early investigations explored wavy channels through two-dimensional computational modeling of laminar flow [4–8]. These groups identified that the flow along the wall, even while in the low Reynolds number regime, would detach and develop a vortex in the cavity between waves. Nishimura et al. [7] investigated this phenomenon in a converging–diverging wavy channel and found that the size of the recirculation zones were a function of Reynolds number. These zones increase in size with increases in Reynolds number for laminar flows, but after the flow transitions to turbulence, these recirculation zones reduce in size to a limiting value with continued increases in Reynolds number. Snyder et al. [9] expanded on these findings, identifying that this detachment and recirculation resulted in local heat transfer augmentations with levels being periodic along a wavelength. The location of highest heat transfer enhancements coincided with the lowest wall shear stress, which occurred just downstream of the flow detachment.

As studies of these channels grew more sophisticated, three-dimensional computational domains were used more often to understand the unique flow features. Comini et al. [10] explored how the

<sup>1</sup>Corresponding author.

Contributed by the International Gas Turbine Institute (IGTI) of ASME for publication in the JOURNAL OF TURBOMACHINERY. Manuscript received July 28, 2022; final manuscript received August 31, 2022; published online October 20, 2022. Tech. Editor: David G. Bogard.

aspect ratio of a wavy channel impacted performance, finding that in the laminar regime dean vortices developed whose magnitude was a function of channel aspect ratio. These dean vortices enhanced local heat transfer by moving fluid from the wall into the channel center. These findings were later validated by Sui et al. [11], who conducted a study with channels of varying relative waviness and showed the development of dean vortices. Siu et al. also noted that this enhancement was accomplished with minimal increases to pressure drop, making wavy channels a potential cooling technology.

Recent studies have continued to investigate geometric variations of wavy channels [12] still focusing on the performance in the laminar regime. Several studies were conducted by Hari Krishnan and Tiwari [13,14] investigating the performance of 3D wavy channels who found secondary flows enhanced heat transfer in the valleys of a wave, but the greatest heat transfer occurred at the crest of a wave due to reattachment. Lin et al. [15] found that by modulating the amplitude and wavelength of a wavy channel along the flow length, it was possible to increase the magnitude of the dean vortices and improve heat transfer. Further investigations of amplitude and wavelength were completed by Zhou et al. [16], who showed how channels with high amplitudes or low wavelengths induced strong vortices in the pits of the wave, enhancing heat transfer at a high pressure cost.

AM offers the ability to integrate novel cooling designs, such as wavy channels, into gas turbine components easier than ever before, as shown by Wimmer et al. [17]. Integration, however, presents new complications that are not present in traditional manufacturing. An initial study from Kirsch and Thole [18] investigated both the feasibility of constructing AM wavy microchannels as well as heat transfer and pressure loss performance. Much like previous AM microchannel studies [19,20], they found that the channel surfaces had a high roughness relative to their hydraulic diameter and, due to their size, were difficult to post-process. Convective heat transfer was enhanced significantly by the roughness especially at high Reynolds numbers.

Previous studies highlighted the impact that additive roughness has on the performance of wavy microchannels, and the unique

flow features that develop as a function of channel geometry, but questions still remain. This study aims to address one such question by methodically investigating how the amplitude and wavelength of AM wavy microchannels impact performance over a range of Reynolds numbers.

## Description of Test Coupons

Five flat test coupons were additively manufactured for this study, as shown in Fig. 1, that were similar in construction to test coupons used in prior studies by one of the co-authors [21]. The specific dimensions and characteristics of each of the coupons can be seen in Table 1. Each coupon was designed to be 50.8 mm long, 25.4 mm wide, and have a total thickness of 3.05 mm. Channel lengths were defined along the centerline of the channel and were over 40 hydraulic diameters long to minimize entrance effects, and varied in total length due to changes in the channel amplitude or wavelength. Between seven and nine wavy channels were packaged into each coupon depending upon the geometry. Each channel had an aspect ratio of 1:2 with a height of 1.91 mm. These dimensions resulted in a channel hydraulic diameter of 1.27 mm.

A nominal wavy channel was defined with a given amplitude and wavelength, with the cross section of the channel being kept constant along the flow direction as shown by the dashed line in Fig. 2. In addition to this nominal case, four more designs were developed by varying the amplitude or wavelength of the channel resulting in the test matrix seen in Fig. 2. The colors illustrating these designs are consistent throughout the entirety of the paper when reporting the data in later sections.

The five coupons were manufactured using DMLS using an EOS M280 printer. The coupons were manufactured out of Hastelloy-X, using the process parameters recommended by the manufacturer. This material was selected based on its prevalence to gas turbine components so as to accurately capture inherent roughness effects.

The coupons were manufactured in a vertical orientation, where the build direction was along the length of the coupon. Supports were used for the top flange and to anchor the parts to the build plate. Following the build, the parts were cleared of powder, heat treated to relieve thermal stresses, and machined by wire electric discharge machining (EDM) to remove supports and extract the parts from the build plate. Computed tomography (CT) scans showed that the powder was removed from the channels.

During coupon testing, it was discovered that for the shortest wavelength coupon ( $0.5\lambda$ ), the heat transfer was so high that the flow temperature thermally saturated resulting in high uncertainties. To avoid saturation, the test coupon was shortened for the  $0.5\lambda$  wavelength design. Comparisons of pressure loss data taken with both the shorter and longer coupon for this geometry compared well. The shorter coupon is shown in Table 1 as  $0.5\lambda$ -Mod and was used for all heat transfer tests.

## Channel Characterization

To accurately capture the geometric characteristics inside the channels non-destructively, as well as to quantify the roughness on the interior coupon surfaces, each of the coupons underwent

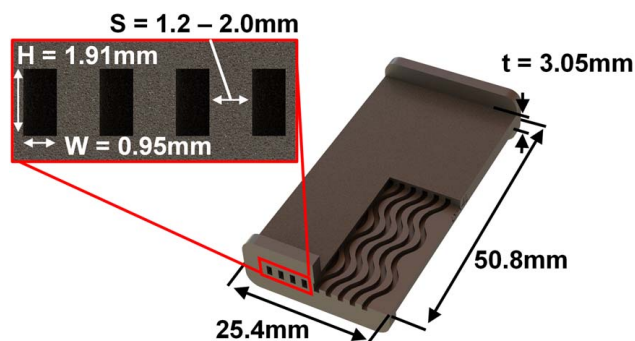


**Fig. 1** Dimensioned test coupon used to determine the friction factor and bulk Nusselt number of the wavy channels with internal geometry exposed

**Table 1** Coupon geometric characteristics

Coupon name	Amplitude (mm)	Wavelength (mm)	Measured $D_h$ (mm)	Channel length (mm)	Number of channels	Design surface area ( $m^2$ )	Measured surface area ( $m^2$ )	$R_a$ ( $\mu m$ )	$R_a/D_h$
0.5 A	1.0	10.2	1.20	52.1	8	0.00238	0.00240	14.3	0.0120
$0.5\lambda$	2.0	5.1	1.21	69.9	7	0.00280	0.00272	20.7	0.0171
$0.5\lambda$ -Mod	2.0	5.1	1.21	34.7	7	0.00139	0.00135	20.7	0.0171
Nominal	2.0	10.2	1.23	56.8	9	0.00292	0.00287	15.9	0.0130
$1.5\lambda$	2.0	15.2	1.27	53.2	8	0.00243	0.00230	16.2	0.0128
$1.5\lambda$ A	3.0	10.2	1.21	62.2	8	0.00284	0.00276	15.4	0.0127

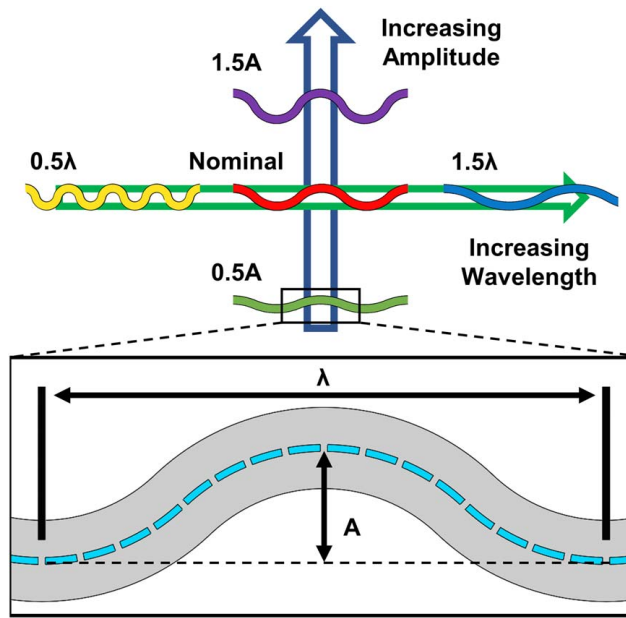


**Fig. 2 Test matrix description and amplitude and wavelength definitions for wavy channels**

CT scans. The scans were completed using a voxel size of  $35\ \mu\text{m}$ , which was then further resolved using a commercial software, enabling the determination of the surface of the coupon to one-tenth the voxel size or  $3.5\ \mu\text{m}$  [22].

Arithmetic mean roughness ( $R_a$ ) measurements were calculated using a method similar to that described by Stimpson et al. [19], wherein the roughness is representative of the average deviation of a surface from a reference. The values from several measurements were combined using a surface area average for each coupon and is reported in Table 1.

The roughness for the internal channel surfaces ranged between  $14 < R_a < 21\ \mu\text{m}$ , which matched similar levels of surface roughness for a vertical build orientation as seen by Wildgoose et al. [21]. Notably, the shortest wavelength coupon had the highest measured  $R_a$ , which was likely a result of the increased number of downskin surfaces.

To capture the hydraulic diameter ( $D_h$ ) of each of the channels, the coupon surfaces were exported from the CT software and analyzed using an in-house code. This code sectioned the channels into over 900 slices along their flow direction from which an average channel perimeter and cross-sectional area for each slice were calculated. These values were then averaged over all slices for a given coupon to find the average hydraulic diameter for the coupon, which is reported in Table 1. The measured hydraulic diameter was consistently close to the design with a maximum deviation of 5%.

## Experimental Methods

A test rig was constructed to experimentally evaluate the performance of the coupons over a range of Reynolds numbers. The test rig used was similar in construction to that used by Stimpson et al. [19] as illustrated in Fig. 3.

Each coupon was installed between two plenums to ensure that the flow entering and leaving the coupon was uniform. Air entering the test section was metered using a mass flow controller located upstream and pressure in the test section was regulated through a needle valve located downstream allowing for independent control of the Reynolds number and Mach number. Each plenum was fitted with a pressure tap to capture the pressure drop across the coupon using a differential pressure transducer with swappable diaphragms to capture different pressure ranges. An additional

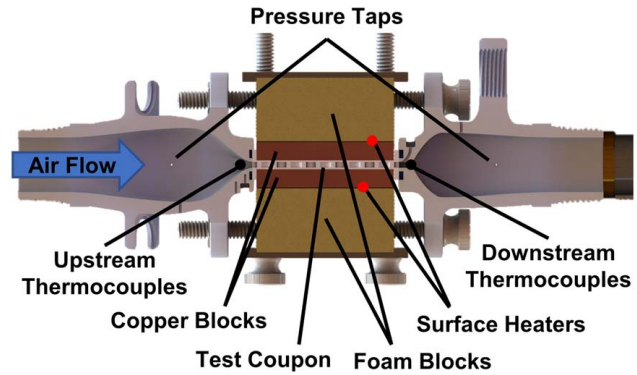


**Fig. 3 Cross section of test rig used to evaluate coupon heat transfer and friction factor performance**

gauge pressure sensor was fitted to the upstream pressure tap to capture the operating pressure.

For the heat transfer tests, a heating assembly was placed on both sides of the test coupons. Each assembly consisted of a custom-built heater installed between a foam block and a copper block. Each heater was connected to its own power supply, allowing for independent control of the heat applied to each side of the coupon. The copper blocks interfaced with the test coupon, with a thin layer of thermal paste applied between the two components to minimize conductive resistance. The heat lost to components surrounding the coupon was determined by calculating 1D losses from thermocouple measurements in the foam blocks and plenums. These losses were typically at or less than 1% of the total heat input into the system for all heat transfer tests. The copper blocks were fitted with several precisely placed thermocouples to determine the surface temperature of the coupon using a 1D conduction analysis as described by Stimpson et al. [19]. The thermal conductivity of the Hastelloy-X test coupons was measured to be  $10.0\ \text{W/m K}$ .

The temperature of the air upstream and downstream of the coupon was captured with additional thermocouples placed into the flow just upstream and downstream of the test coupon. The system was required to reach steady state while testing, which was determined by monitoring a time resolved plot of temperatures. An iterative calculation assuming 1D isentropic flow was used to accurately determine the temperature, pressure, velocity, and density of the air at the inlet and exit of the test coupon. The coupon surfaces were assumed to be isothermal based on calculated high fin efficiencies. The bulk convective coefficient and Nusselt number were calculated using the coupon surface temperature, as seen in Eq. (1).

$$h = \frac{Q_{\text{in}} - \sum Q_{\text{loss}}}{A_s \cdot \Delta T_{\text{lm}}} \quad (1)$$

To ensure all the energy in the system was captured, an energy balance was conducted by comparing the total heat input minus losses to that measured using a first law analysis. The energy balance for low Reynolds number tests were within 5% with some of the tests at high Reynolds numbers having a balance within 8%.

As an additional measure, the test procedures and facility were benchmarked against known correlations using a smooth-walled coupon featuring straight circular channels. Friction factor measurements during benchmarking were compared to the Colebrook correlation in the fully turbulent regime seen as Eq. (2) [23].

$$\frac{1}{\sqrt{f}} = -2 \log_{10} \left( \frac{k_s}{3.7D_h} + \frac{2.51}{\text{Re}\sqrt{f}} \right) \quad (2)$$

Note that it was expected that the benchmarking machined coupon's surface roughness,  $k_s$ , was zero. By iteratively solving



the Colebrook equation with this assumption, the friction factor for a smooth channel was then defined as  $f_0$ , which was used for the augmentation factors.

Heat transfer measurements were similarly taken using the same benchmarking coupon and compared against the Gnielinski correlation, which is shown in Eq. (3) [24].

$$Nu = \frac{(f/8)(Re - 1000)Pr}{1 + 12.7\sqrt{f/8}(Pr^{2/3} - 1)} \quad (3)$$

The smooth channel Nusselt number,  $Nu_0$ , was then found by solving the Gnielinski correlation with  $f_0$  over a range of Reynolds numbers, which was also used for augmentations.

## Measurement Uncertainty

Measurement uncertainty was determined using the methods as described by Dunn [25]. Friction factor measurements were found to have a high uncertainty in the low Reynolds regime, at just over 20% of measured value with the main contributors being the differential pressure measurement and the mass flowrate. After a Reynolds number of 5000, all measurements were within a 5% uncertainty. During testing, several friction factor data points were collected multiple times for each coupon using different differential pressure sensor diaphragms and identified that pressure drop results were repeatable to within 3% of the full-scale value.

Nusselt number uncertainty was similarly calculated, and it was found that the relative uncertainty of Nusselt number was less than 8% with the main contributors being thermocouple measurements at the exit of the test coupon and the temperature measured in the copper blocks. Additional heat transfer measurements were made to evaluate repeatability, and found that the measured Nusselt number was repeatable within 2%.

## Computational Methods

A CFD simulation was conducted for each of the five channel geometries previously discussed. The objective of this analysis was to identify any driving flow features that impacted the heat transfer and friction factor performance of the channels within the study. The CFD domain shown in Fig. 4 was modeled for these comparisons. It was assumed that the coupon wall temperature was constant due to high fin efficiency. A symmetric boundary

condition was applied to the top wall and the channel lengths were increased by a factor of 2.5 to better understand the thermal saturation. Modeling AM roughness computationally has been shown previously to be difficult [26]. As such, the channel walls were assumed to be smooth, as the CFD was intended to provide a relative comparison rather than be fully representative of the as-built channel performance.

A mass flow inlet was imposed on the entrance of each of the channels, with a flowrate set to achieve a Reynolds number of approximately 10,000. An outflow boundary condition was imposed at the channel exit. For the CFD simulations, the inlet velocity profile was considered uniform given the plenum used in the experiment accelerated the flow and flattened the profile.

The density of the air was assumed to be constant based on a testing relevant pressure and temperature. The simulations were solved by approximating the solution to the Reynolds-averaged Navier–Stokes equations using a commercial CFD solver [27]. The pressure–density coupling scheme was semi-implicit method for pressure linked equations (SIMPLE), and all spatial equations were resolved to second order. Turbulence was modeled using the realizable  $k$ – $\epsilon$  model, and heat transfer at the wall was modeled using enhanced wall treatment. Prior studies by one of the co-authors [18,28] have shown that while secondary flows may be moderately underpredicted using the realizable  $k$ – $\epsilon$  model, the relative performance between channels is captured.

The grids used to model the channels were created using a commercial grid generation software [29]. Structured grids were generated with a value of  $y^+ \sim 1$  in the near-wall regions. The grid size between the trails varied, but the total number of cells for each case was near 3.5 million elements. A mesh-sensitivity study was conducted using increasing mesh sizes from 1.5 million to well over 8 million elements. Increasing the cell count from 3.5 million to 8 million yielded a change in friction factor and Nusselt number results of less than 1%.

The simulation was considered converged when the outlet temperature remained constant over 200 iterations and all normalized residuals were below  $10^{-6}$ .

## Effect of Channel Wavelength

The measured pressure losses in terms of friction factors for coupons of varying wavelengths at a constant amplitude are seen

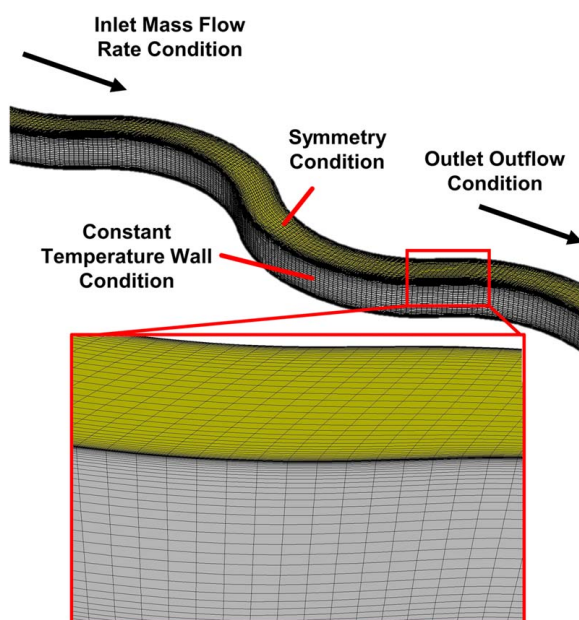


Fig. 4 Example of domain used in computational study

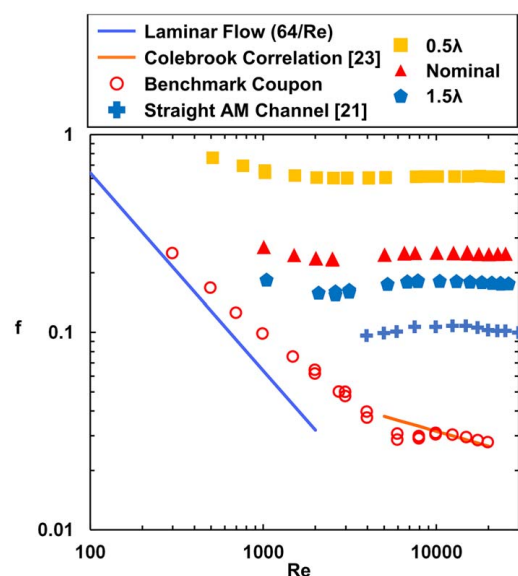
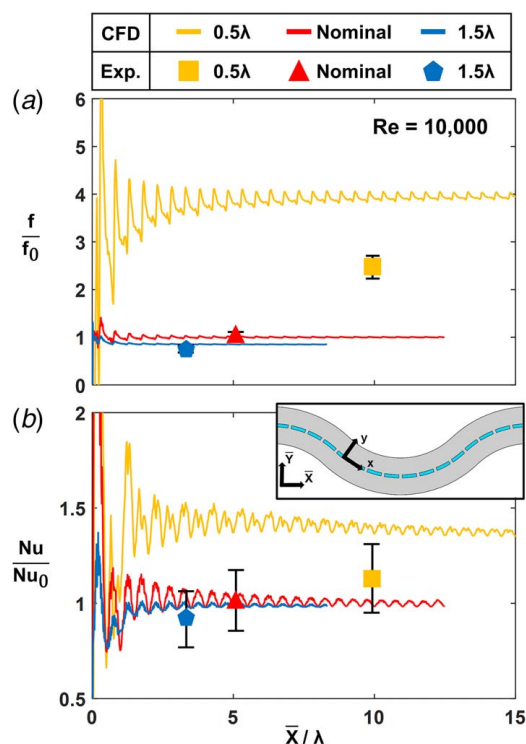


Fig. 5 Friction factor testing results for channels of varying wavelength and constant amplitude as a function of channel Reynolds number

in Fig. 5. Also shown in Fig. 5 is the data from a coupon used for benchmarking the test rig and data for a straight AM channel with a similar hydraulic diameter and relative roughness ( $D_h = 1.25$  mm and  $R_a = 12$   $\mu$ m) [21]. These results indicate that all wavy channels have a much higher friction factor than both the smooth and additively manufactured straight channels. The results also indicate that decreased wavelength results in substantially increased friction factors. As the wavelength decreases, the increased friction factor is caused by increased flow detachment and reattachment as the flow passes over increasingly steep convex walls. The data in Fig. 5 also indicate that the friction factor for the wavy channels becomes independent of Reynolds number as early as  $Re \sim 2000$ , as compared with  $Re \sim 10,000$  for the rough straight channels. This independence is typically associated with highly turbulent flows indicating impacts of roughness and turbulence.

To understand the impact that the channel geometry has on performance, the predicted local friction factor and Nusselt number were calculated from the simulations as shown in Fig. 6. Note that these results are presented as augmentations from the nominal case, whereby  $f_n$  and  $Nu_n$  are the average of the values predicted for the nominal case after 10 wavelengths for the computational results and the experimental value of the nominal case for the experimental results. Using this normalization, the nominal case in Fig. 6 oscillates about unity as would be expected. The  $x$ -axis in Fig. 6 is the global  $x$ -coordinate,  $\bar{X}$ , normalized by the channel wavelength,  $\lambda$ . Using this coordinate system aligns the wave of each channel making it possible to compare performance along a wavelength.

In Fig. 6(a), there is a periodic nature to the friction factor results due to the channel wave. The peaks were co-located near the flow attachment, whereas the valleys are co-located near the flow detachment. The peaks are most pronounced for the low wavelength case ( $0.5\lambda$ ), given that the channel requires the most aggressive changes to flow direction. The periodic behavior occurs through the developing region of the flow with the oscillations damping to nearly constant peak and valley values after approximately  $L/D_h \sim 30$  (or



**Fig. 6** (a) Friction factor augmentation and (b) Nusselt number augmentations as compared to the nominal case for channels of varying wavelength and constant amplitude

$7.5\lambda$ ) for the low wavelength case ( $0.5\lambda$ ). In the highest wavelength case ( $1.5\lambda$ ), the oscillations dampen after only  $L/D_h \sim 20$  ( $1.25\lambda$ ). While Fig. 6(a) illustrates that the CFD significantly overpredicted the relative increase in friction factor for the low wavelength case ( $0.5\lambda$ ), the predictions for both the nominal and  $1.5\lambda$  cases are relatively good. It is likely that this disagreement between the computational and experimental data is due to the realizable  $k$ - $\epsilon$  model inaccurately capturing the near-wall behavior as was seen in the shortest wavelength case. However, the same trends were found between measured and predicted data.

Experimentally obtained heat transfer data from coupons of varying wavelength at a constant amplitude are shown in Fig. 7. Also shown is the benchmark data for smooth channels and heat transfer measurements for the same straight AM channel presented in Fig. 5. A similar trend was seen to that of the friction factor results, where the decreased wavelength resulted in increased Nusselt numbers. Particularly, the Nusselt number for the nominal and increased wavelength ( $1.5\lambda$ ) was nearly the same at high Reynolds number. Also shown in Fig. 7 is the notable increase in heat transfer over the straight AM channel, demonstrating how even moderately wavy channels can induce significantly increased heat transfer.

Evaluating the local Nusselt number in Fig. 6(b) reveals a similar oscillatory structure in the heat transfer, as was seen with the friction factor, where the detachment and reattachment of the fluid on the crests of a wave resulted in high heat transfer regions. The peak and valley behavior of heat transfer occurs because the heated flow along the wall mixes into the cooler channel flow towards the center as it detaches from the wave with cooler fluid replacing it from the central flow region upon reattachment. Similar to the friction factor data, the CFD overpredicted the heat transfer for the low wavelength ( $0.5\lambda$ ) channel but gave reasonable predictions for the others.

The predicted thermal profiles across the entire channel can be seen in Figs. 8(a)–8(e), with Figs. 8(b), 8(c), and 8(d) representing the low ( $0.5\lambda$ ), nominal, and high ( $1.5\lambda$ ) wavelength cases for the same amplitude. The predictions show decreasing the wavelength of the channel results in higher heat transfer to the working fluid, which is consistent with the experimental Nusselt number data. These results show that the shortest wavelength coupon, Fig. 8(b), becomes thermally saturated at the full coupon length,

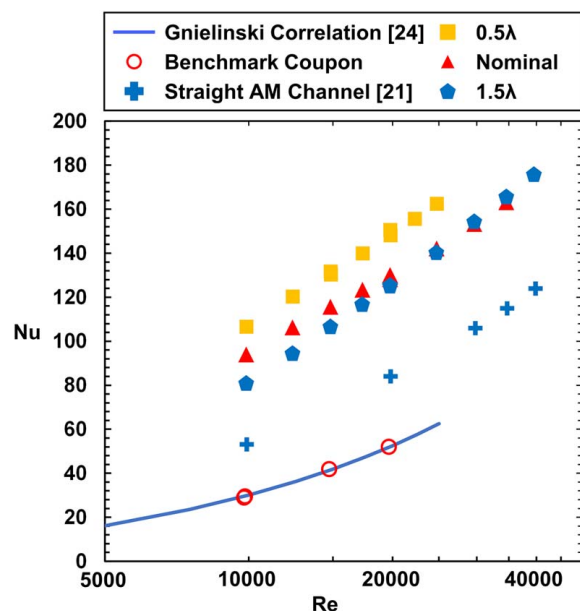


**Fig. 7** Nusselt number as a function of Reynolds number for coupons of varying wavelength and constant amplitude in the turbulent regime

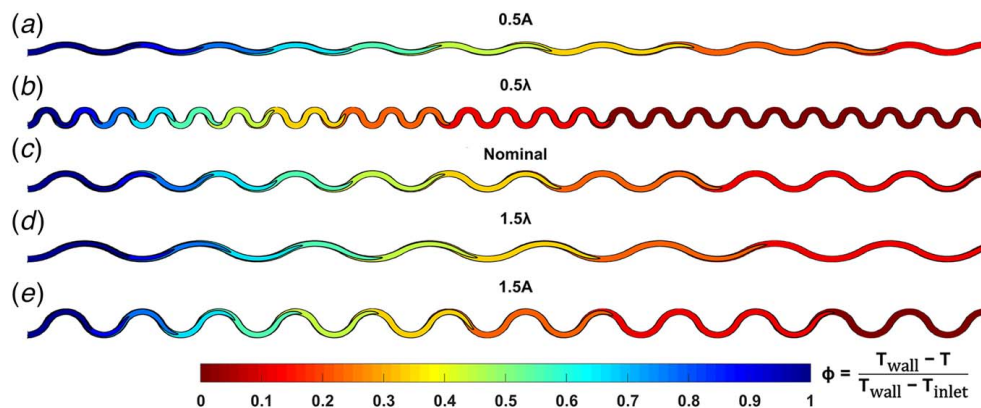


Fig. 8 (a)–(e) Thermal contours for the tested channels normalized by the inlet and wall temperatures

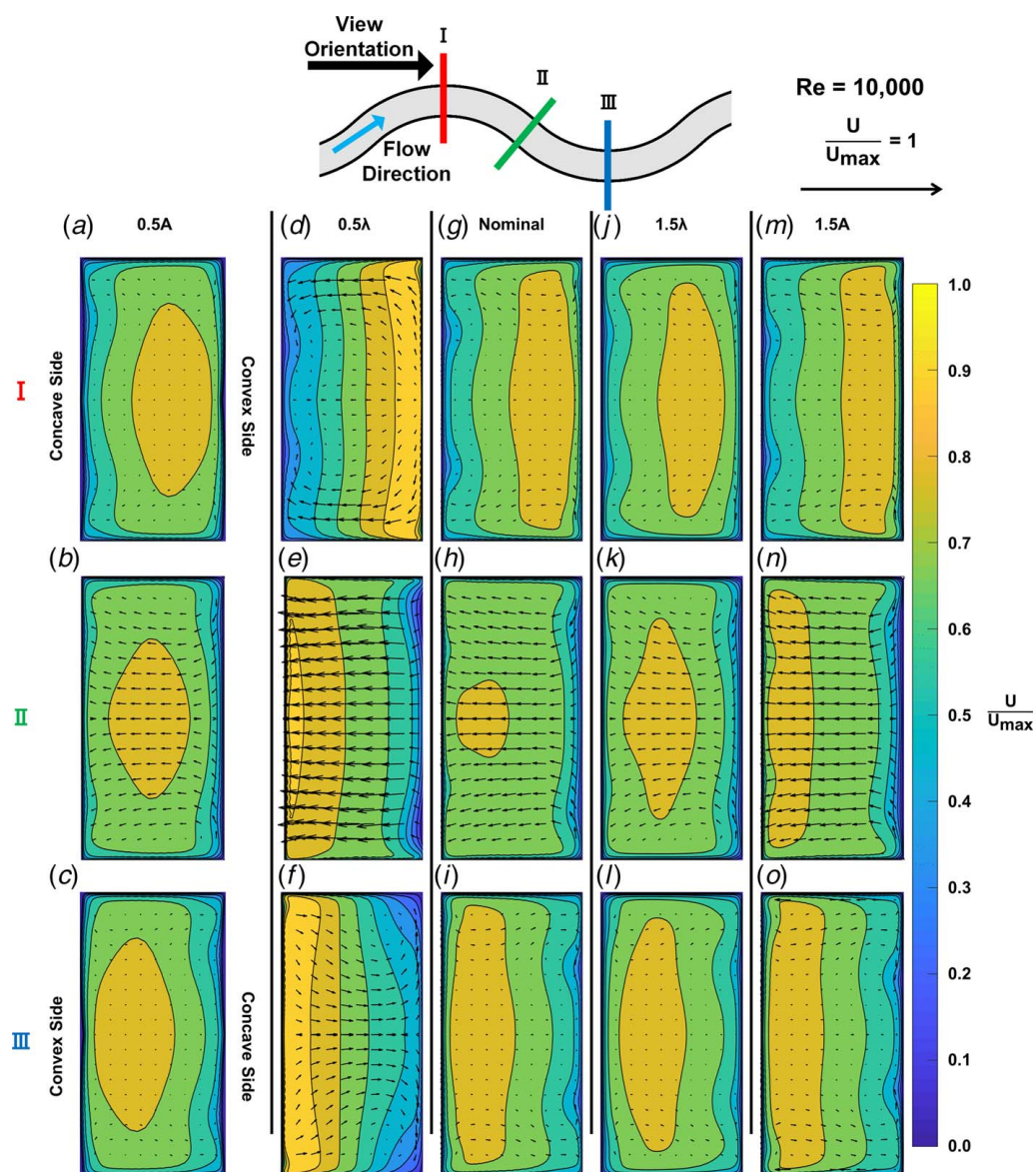


Fig. 9 Normalized maximum velocity and secondary flows at three planar locations along a given wavelength for the reduced amplitude (a)–(c), reduced wavelength (d)–(f), nominal (g)–(i), increased wavelength (j)–(l), and increased amplitude (m)–(o) cases



also matching experimental results. The predicted heat transfer trends between channels also match the results shown in Fig. 7, in that the nominal and high wavelength cases, shown as Figs. 8(c) and 8(d), respectively, had very similar thermal pickup.

To further investigate this periodic structure, the velocity fields predicted by the CFD were captured at three different planar locations for each of the five wavelengths as presented in Figs. 9(a)–9(o). The concave and convex sides of the channel are annotated for the first channel in a row, but are true for the remaining channels in the row. The low ( $0.5\lambda$ ), nominal, and high ( $1.5\lambda$ ) wavelength cases are presented in Figs. 9(d)–9(f), 9(g)–9(i), and 9(j)–9(l) for the same amplitude. The velocity contours show that the distribution of the flow shifts towards the convex side of the channel as wavelength decreases. This change in the flow distribution results from the pressure gradients that form along the steep convex walls of the channel similar to large ribs.

Figures 9(d), 9(g), and 9(j) show distribution of secondary flows at the first planar location for the three channels in the order of increasing wavelength. The secondary velocities indicate that the magnitude increases with decreasing wavelength. The secondary flow structures change as a function of wavelength as shown in Figs. 9(g) and 9(j), which indicate the development of two pairs of dean vortices along the concave wall and in the corners of the convex wall of the wave. One pair of the dean vortices is not present in the low wavelength case ( $0.5\lambda$ ) as shown in Fig. 9(d). For the low wavelength case in Fig. 9(d), the secondary flows develop into two large cells that occupy the top and bottom of the channel. In the second planar location, mid-way between the peak and valley, Figs. 9(e), 9(h), and 9(k), indicate that there are almost no vortices as the flow shifts from one curved wall to the other. The planar location at the valley of the curve, shown as Figs. 9(f), 9(i), and 9(l) for the low ( $0.5\lambda$ ), nominal, and high ( $1.5\lambda$ ) wavelength cases, also indicates that the flow is completely mirrored between the first and last planar locations. The secondary flows exhibited in the channels of varying wavelength, Figs. 9(d)–9(l), improved heat transfer in the channels computationally; however, it is expected that the surface roughness will have a more significant impact on the heat transfer of the channel, as seen by prior researchers [18].

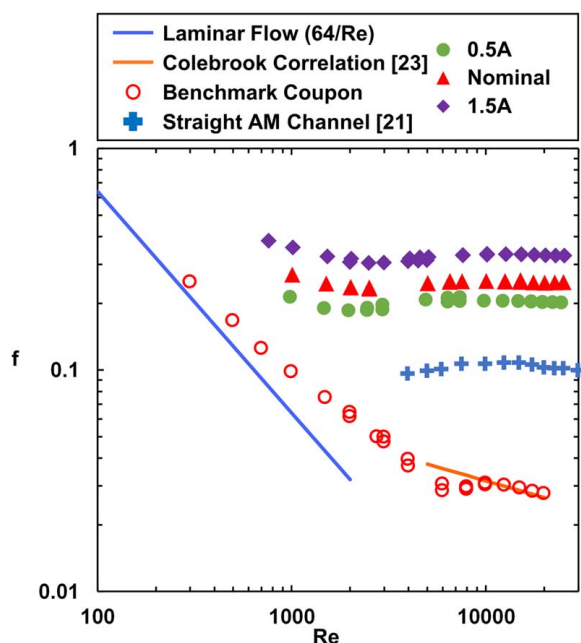


Fig. 10 Friction factor as a function of Reynolds number for channels of varying amplitude and constant wavelength

## Effect of Channel Amplitude

The friction factor results from coupons of varying amplitude at a constant wavelength can be seen in Fig. 10. The influence of amplitude was found to be the inverse of wavelength with higher amplitudes resulting in increased friction factors. Given that increased pressure loss is largely a function of the flow detaching and attaching from the inside walls of the channels, it is expected that increasing amplitudes resulted in higher friction factors. Similar to Fig. 5 for different wavelengths, Fig. 10 also indicates that the friction factor of the wavy channels becomes independent of Reynolds number at low values ( $Re \sim 4000$ ) relative to that of the smooth coupon.

Predictions of the development of the local friction factor and Nusselt number augmentation relative to the nominal case along the channel length are shown in Fig. 11. Two conclusions can be drawn from Fig. 11(a): the amplitude of the oscillations present in the friction factor results is dependent on the wave amplitude and the CFD predictions were correct in trend but slightly off in comparing the average bulk values. Increasing channel amplitude results in increases to the amplitude of the periodic behavior in friction factor, as well as streamwise length required for the periodic behavior to reduce to the fully developed value. These results for the changing amplitude differ from the modifications to wavelengths over which we studied, where changes in friction factor from the nominal case were found to be significantly higher when wavelength was changed.

Figure 11(b) shows the local development of Nusselt number, where it can be seen that the CFD predictions were close to the measured average heat transfer. Similar to the friction factor predictions, the amplitude of the oscillations in heat transfer are smaller for the decreased amplitude case ( $0.5A$ ) as compared to the increased amplitude case ( $1.5A$ ). Based on the predictions, the influence of the wave amplitude on the oscillations is lower than that of the wavelength for the ranges studied.

The experimentally obtained Nusselt number for the coupons of varying amplitude over the entire Reynolds number range is shown

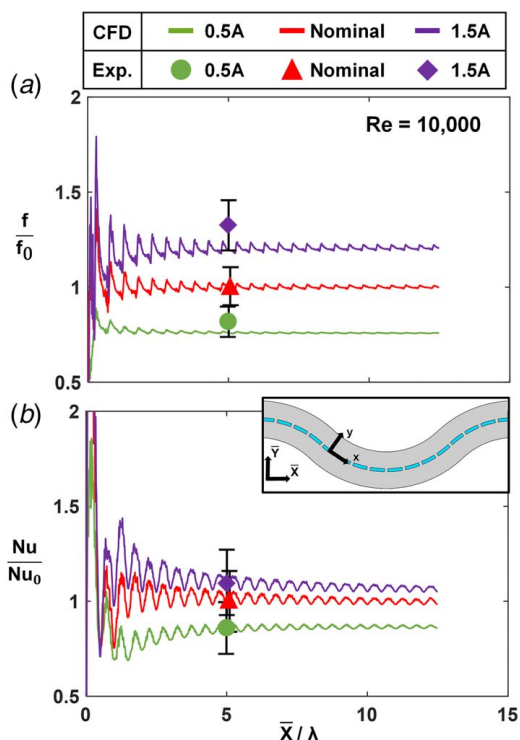


Fig. 11 (a) Friction factor and (b) Nusselt number augmentations from the nominal case for channels of varying amplitude and constant wavelength

in Fig. 12. The highest amplitude channel (1.5 A) achieved the highest Nusselt numbers throughout the test range. The heat transfer performance of the channels approached similar values at the highest Reynolds number tested for the highest amplitude case (0.5 A) and the nominal case. These results align well with the assumption that the increased protrusion of the convex walls into the main channel flow results in increased flow mixing and subsequent heat transfer, as seen in the channels of varying wavelength. The impact of this change can be seen in Figs. 8(a), 8(c), and 8(e), where the thermal contours for the decreased (0.5 A), nominal, and increased (1.5 A) amplitude cases can be seen. Opposite to the channels of varying wavelength, there is a clear trend of increased fluid temperatures as the channel amplitude increases, matching experiments.

The velocity contours presented in Fig. 9 with the channels of varying amplitude are displayed in Figs. 9(a)–9(c), 9(g)–9(i), and 9(m)–9(o). Similar to changing wavelength, the peak velocities shift between the convex walls as the fluid passes through the channel, which is also apparent for the smallest amplitude case (0.5 A) represented in Figs. 9(a)–9(c). This shift becomes more pronounced with increasing amplitude, shown in Figs. 9(m)–9(o), where the flow is largely hugging the convex channel wall regardless of streamwise location resulting from the cross-channel pressure gradient. There is a less pronounced impact on the development of the secondary flows as compared to changing wavelength over the ranges studied with very similar formations of dean vortices for all the amplitudes as shown by Figs. 9(a), 9(g), and 9(m). Similar to decreasing wavelength, increasing channel amplitude increased the magnitude of the secondary flows, as seen in Figs. 9(c), 9(i), and 9(o).

## Overall Channel Performance

To scale the relative performance of all the wavy channels, a parameter previously recommended by Sui et al. [11] was evaluated. Sui et al. suggested the use of a relative waviness parameter, defined as the channel amplitude divided by the channel wavelength. Figures 13(a) and 13(b) show the performance augmentation with respect to a smooth coupon for both friction factor and Nusselt number augmentations as function of relative waviness

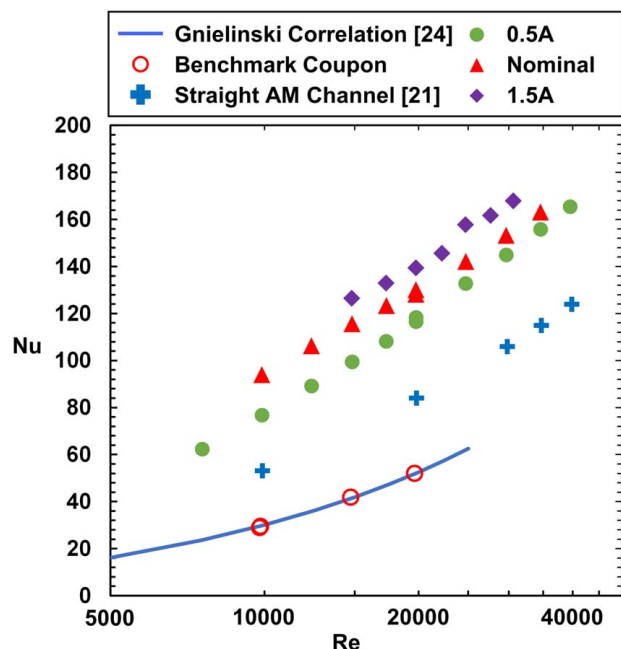


Fig. 12 Nusselt number for channels of varying amplitude and constant wavelength as a function of channel Reynolds number

for three Reynolds numbers. The dashed lines in both Figs. 13(a) and 13(b) are intended to represent the general performance trend and is not representative of any correlation. Straight AM channel data are also plotted in Figs. 13(a) and 13(b) ( $A/\lambda = 0$ ) for reference. At a Reynolds number of  $Re = 30,000$ , the friction factor augmentation shows a strong functional increase as  $A/\lambda$  increases, which results from the increased obstruction of the convex wall into the flow path resulting in increasing pressure losses. These trends in friction factor are the same as Reynolds number is decreased, though the magnitude of the friction factor augmentation decreases.

The augmentations to heat transfer in Fig. 13(b) at a Reynolds number of  $Re = 30,000$  show only a slight increase with  $A/\lambda$ , nearly flattening as  $A/\lambda$  approaches 0.5. As Reynolds number is decreased however, there is an apparent trend of increased heat transfer as relative waviness is increased. This aligns with what was seen previously in Figs. 7 and 12, as all tested channels approached similar Nusselt number values as the Reynolds number was increased. These results imply that for some cases there is a diminishing impact for turbine cooling relative to pressure loss.

To capture these cases of diminished cooling, two methods were used to compare the overall performance of the channels. The first

Re	0.5A	0.5λ	Nominal	1.5λ	1.5A	Straight Channel [21]	Trendline
10k	○	□	△	◇	◇	+	---
20k	●	■	▲	◆	◆	+	---
30k	⊗		▲	◆	◆	+	---

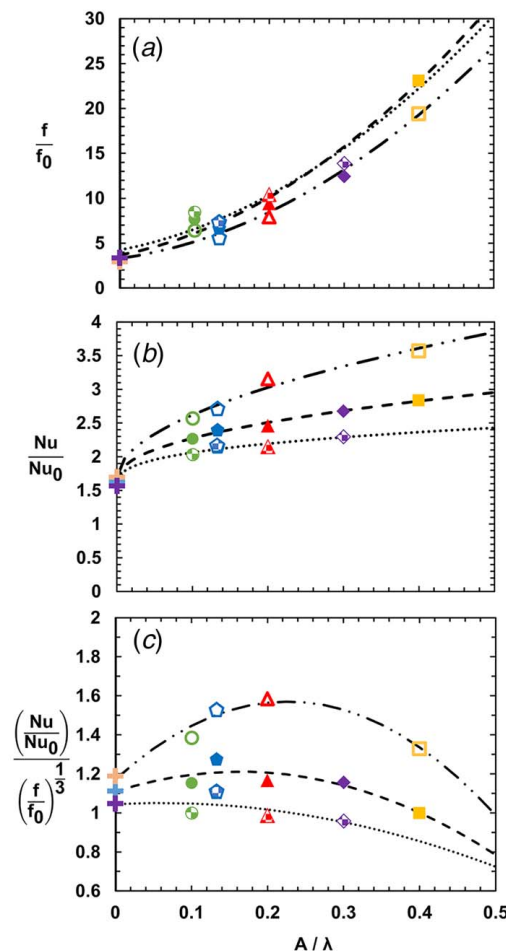


Fig. 13 (a) Friction factor augmentation, (b) Nusselt number augmentation, and (c) efficiency index as a function of channel relative waviness



used the efficiency index, as described by Eq. (4).

$$I = \frac{(Nu/Nu_0)}{(f/f_0)^{1/3}} \quad (4)$$

The efficiency index is an indicator of the heat transfer performance enhancement relative to the required increase in pumping power and was adapted from previous studies [30]. The efficiency index is plotted as a function of the relative waviness in Fig. 13(c). It is clear from this figure that the efficiency index for channels of a relative waviness of less than  $A/\lambda = 0.3$  was similar for Reynolds number of 20,000 and 30,000. This is not true for the coupons tested at a Reynolds number of 10,000, where the increases in heat transfer seen in Fig. 13(b) outweighed the frictional losses shown in Fig. 13(a), particularly for the relative waviness range of  $0.1 < A/\lambda < 0.3$ . There was a decrease in performance across all Reynolds numbers after a waviness of  $A/\lambda > 0.3$ , as the increased frictional losses were met with only minor increases in heat transfer as was seen in Fig. 13(b). As the Reynolds number was increased, it should also be noted that the efficiency index continued to decrease, and almost all wavy channels at a Reynolds number of  $Re = 30,000$  had a smaller efficiency index than a straight microchannel, indicating that wavy channels would be most effective in a Reynolds number range of  $5000 < Re < 10,000$ .

The second method to compare the overall performance of the channels was to compare the Nusselt augmentation for a given friction factor augmentation across the tested designs. The augmentations with respect to a smooth coupon are presented in Fig. 14 for all Reynolds numbers. These results showcase the wide range of performance available from channels of varying amplitude and wavelength. Notably, channels that had a small amplitude (0.5 A) and high wavelength (1.5λ) saw similar performance throughout the testing range whereas high amplitudes (1.5 A) and low wavelengths (0.5λ) saw substantial increases in friction factor for notable increases in Nusselt augmentation. The performance of wavy channels relative to a straight AM channel is also presented on this plot where it can be seen that any level of channel waviness was found to substantially increase both friction factor and Nusselt number. Note that the straight AM channel is still affected by the channel roughness, which is why the augmentations are above one.

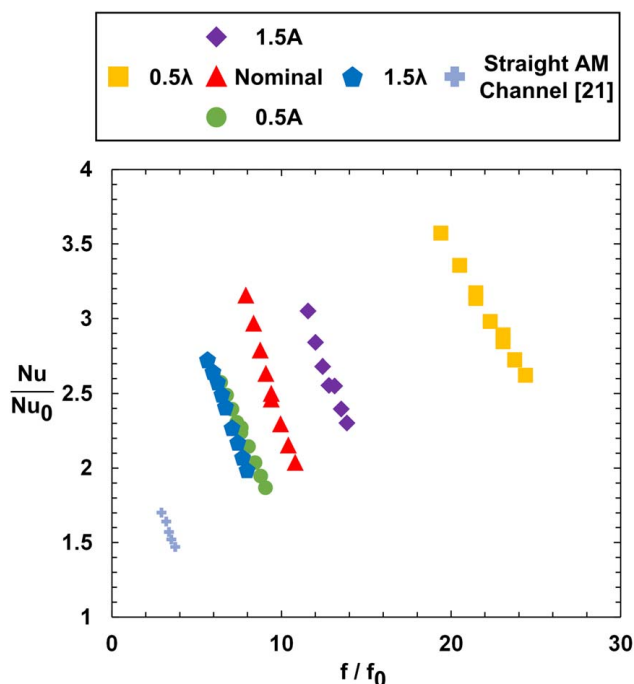


Fig. 14 Nusselt number augmentation as a function of the friction factor augmentation for all channels

## Conclusions

This study investigated how the amplitude and wavelength of additively manufactured wavy channels impact heat transfer and pressure loss using experimental testing and CFD predictions. Test coupons were additively manufactured using direct metal laser sintering and were then analyzed using CT scans to determine the accuracy to the design intent and investigate internal surface roughness.

Coupon characterization showed that when built vertically, the channel shape and diameter were manufactured with only slight variations relative to the design intent. The roughness was found to be similar across all coupons, except for the shortest wavelength case, which saw a notable increase because of the increased number of downskin surfaces.

The experimental and predicted data indicated that either decreasing channel wavelength or increasing the channel amplitude resulted in increases to both heat transfer and pressure losses. For the friction factor, the data indicated nearly a constant value throughout the range of Reynolds numbers starting as low as  $Re \sim 2000$  indicating a fully turbulent flow.

The friction factor and heat transfer predictions exhibited an oscillatory behavior with decreasing amplitudes of the oscillations when becoming fully developed. The predictions indicated flow detaching and reattaching from the channel surfaces leading to streamwise oscillations in the local friction factors and heat transfer coefficients, which were dependent on both channel amplitude and wavelength. The CFD predictions also elucidated the secondary flows changed considerably with decreasing wavelength while increasing the wave amplitudes resulted in the same secondary flow pattern only stronger vortices.

Scaling the friction factor and Nusselt number data by the relative waviness parameter ( $A/\lambda$ ) showed clear trends in both pressure loss and heat transfer. This scaling indicated that friction factor greatly increased with increasing relative waviness, whereas the heat transfer increased moderately with increasing relative waviness. Due to the high increases in friction factor as compared to the modest increase in heat transfer, the efficiency index was similar for all coupons of low relative waviness, but decreased slightly for the coupon of highest relative waviness. Continued increases in relative waviness would only result in worse efficiency index performance, and the ideal range of relative waviness to maximize heat transfer for a given pumping power is between  $0.1 < A/\lambda < 0.3$ .

This paper uniquely characterized the performance of additively manufactured channels of varying amplitude and wavelength. The data presented in this paper can be used by the gas turbine community to select the best wavy channel configuration for turbine components that require small cooling features, such as blades, vanes, or shrouds. Improved component design can lead to a reduction in required cooling flow, thus resulting in improved overall engine performance.

## Acknowledgment

The authors of this study would like to thank Solar Turbines Incorporated whose support made this work possible. Their insight to the project gave valuable commercial perspective. Additional thanks to Corey Dickman and CIMP-3D for their assistance in developing and printing of AM coupons, as well as Whitney Yetter and Penn State's CQI for conducting all CT scans used to analyze test coupons.

## Conflict of Interest

There are no conflicts of interest.

## Data Availability Statement

The authors attest that all data for this study are included in the paper.

## Nomenclature

- $f$  = Darcy friction factor,  $f = \Delta P(D_h/L)(2/\rho u^2)$   
 $h$  = convective heat transfer coefficient,  
 $h = (Q_{in} - \sum Q_{loss})/A_s \cdot \Delta T_{LM}$   
 $k$  = thermal conductivity  
 $p$  = channel perimeter  
 $u$  = mass average velocity  
 $A$  = channel amplitude  
 $H$  = channel height  
 $L$  = channel length  
 $P$  = static pressure  
 $Q$  = heat transfer rate  
 $T$  = temperature  
 $k_s$  = equivalent sand grain surface roughness  
 $z_{ref}$  = reference surface height  
 $z_{surf}$  = roughness height  
 $A_c$  = cross-sectional flow area  
 $A_s$  = surface area  
 $D_h$  = hydraulic diameter,  $D_h = 4(A_c/p)$   
 $R_a$  = arithmetic mean surface roughness,  
 $R_a = (1/n) \sum_{i=1}^n |z_{surf} - z_{ref}|$   
 $T_{LM}$  = log-mean temperature,  $\Delta T_{LM} = (T_{in} - T_{out})/(\ln((T_s - T_{in})/(T_s - T_{out})))$   
 $y^+$  = dimensionless wall coordinate  
 $Nu$  = Nusselt number,  $Nu = h \frac{D_h}{k_{air}}$   
 $Pr$  = Prandtl number  
 $Re$  = Reynolds number,  $Re = u D_h / \nu$

## Greek Symbols

- $\lambda$  = wavelength  
 $\rho$  = fluid density  
 $\nu$  = kinematic viscosity

## Subscripts

- $in$  = inlet condition  
 $n$  = nominal wavelength/amplitude case  
 $out$  = outlet condition  
 $s$  = surface condition  
 $w$  = wall condition

## References

- [1] IATA, 2021, "Industry Statistics Fact Sheet 2021."
- [2] Ligrani, P., 2013, "Heat Transfer Augmentation Technologies for Internal Cooling of Turbine Components of Gas Turbine Engines," *Int. J. Rotating Mach.*, **2013**, pp. 1–32.
- [3] Manning, R. F., Acquaviva, P. J., and Demers, D. E., 2005, "Gas Turbine Airfoil With Axial Serpentine Cooling Circuits," European Patent EP1001137B1.
- [4] Ahmed, M. A., Shuaib, N. H., and Yusoff, M. Z., 2012, "Numerical Investigations on the Heat Transfer Enhancement in a Wavy Channel Using Nanofluid," *Int. J. Heat Mass Transfer*, **55**(21–22), pp. 5891–5898.
- [5] Guzmán, A. M., Cárdenas, M. J., Urzúa, F. A., and Araya, P. E., 2009, "Heat Transfer Enhancement by Flow Bifurcations in Asymmetric Wavy Wall Channels," *Int. J. Heat Mass Transfer*, **52**(15–16), pp. 3778–3789.
- [6] Wang, G., and Vanka, S. P., 1995, "Convective Heat Transfer in Periodic Wavy Passages," *Int. J. Heat Mass Transfer*, **38**(17), pp. 3219–3230.
- [7] Nishimura, T., Ohori, Y., and Kawamura, Y., 1984, "Flow Characteristics in a Channel With Symmetric Wavy Wall for Steady Flow," *J. Chem. Eng. Japan*, **17**(5), pp. 466–471.
- [8] Xie, G. N., Wang, Q. W., Zeng, M., and Luo, L. Q., 2007, "Numerical Investigation of Heat Transfer and Fluid Flow Characteristics Inside a Wavy Channel," *Heat Mass Transfer*, **43**(7), pp. 603–611.
- [9] Snyder, B., Li, K. T., and Wirtz, R. A., 1993, "Heat Transfer Enhancement in a Serpentine Channel," *Int. J. Heat Mass Transfer*, **36**(12), pp. 2965–2976.
- [10] Comini, G., Nonino, C., and Savino, S., 2003, "Effect of Aspect Ratio on Convection Enhancement in Wavy Channels," *Numer. Heat Transfer Part A*, **44**(1), pp. 21–37.
- [11] Sui, Y., Teo, C. J., Lee, P. S., Chew, Y. T., and Shu, C., 2010, "Fluid Flow and Heat Transfer in Wavy Microchannels," *Int. J. Heat Mass Transfer*, **53**(13–14), pp. 2760–2772.
- [12] Qiao, Z., Wang, Z., Zhang, C., Yuan, S., Zhu, Y., and Wang, J., 2012, "Flow and Heat Transfer in Serpentine Channels," *AIChE J.*, **59**(4), pp. 215–228.
- [13] Harikrishnan, S., and Tiwari, S., 2018, "Effect of Skewness on Flow and Heat Transfer Characteristics of a Wavy Channel," *Int. J. Heat Mass Transfer*, **120**(5), pp. 956–969.
- [14] Harikrishnan, S., and Tiwari, S., 2019, "Heat Transfer Characteristics of Sinusoidal Wavy Channel With Secondary Corrugations," *Int. J. Therm. Sci.*, **145**(4), p. 105973.
- [15] Lin, L., Zhao, J., Lu, G., Wang, X. D., and Yan, W. M., 2017, "Heat Transfer Enhancement in Microchannel Heat Sink by Wavy Channel With Changing Wavelength/Amplitude," *Int. J. Therm. Sci.*, **118**, pp. 423–434.
- [16] Zhou, J., Hatami, M., Song, D., and Jing, D., 2016, "Design of Microchannel Heat Sink With Wavy Channel and Its Time-Efficient Optimization With Combined RSM and FVM Methods," *Int. J. Heat Mass Transfer*, **103**(12), pp. 715–724.
- [17] Wimmer, T., Ruehmer, T., Mick, Y., Wang, L., and Weigand, B., 2019, "Experimental and Numerical Investigation on an Additively Manufactured Gas Turbine Ring Segment With an In-Wall Cooling Scheme," ASME Turbo Expo 2019: Turbomachinery Technical Conference and Exposition, Phoenix, AZ, June 17–21, Paper No. GT2019-90227.
- [18] Kirsch, K. L., and Thole, K. A., 2017, "Heat Transfer and Pressure Loss Measurements in Additively Manufactured Wavy Microchannels," *ASME J. Turbomach.*, **139**(1), p. 011007.
- [19] Stimpson, C. K., Snyder, J. C., Thole, K. A., and Mongillo, D., 2016, "Roughness Effects on Flow and Heat Transfer for Additively Manufactured Channels," *ASME J. Turbomach.*, **138**(5), p. 051008.
- [20] Snyder, J. C., Stimpson, C. K., Thole, K. A., and Mongillo, D., 2015, "Build Direction Effects on Additively Manufactured Channels," *ASME J. Mech. Des.*, **137**(11), p. 111411.
- [21] Wildgoose, A. J., Thole, K. A., Sanders, P., and Wang, L., 2021, "Impact of Additive Manufacturing on Internal Cooling Channels With Varying Diameters and Build Directions," *ASME J. Turbomach.*, **143**(7), p. 071003.
- [22] Reinhart, C., 2011, "Industrial CT and Precision," Volume Graphics GmbH, Heidelberg.
- [23] Colebrook, C. F., Blench, T., Chatley, H., Essex, E. H., Finnicome, J. R., Lacey, G., Williamson, J., and Macdonald, G. G., 1939, "Turbulent Flow in Pipes, With Particular Reference to the Transition Region Between the Smooth and Rough Pipe Laws," *J. Inst. Civil Eng.*, **12**(8), pp. 393–422.
- [24] Gnielinski, V., 1975, "New Equations for Heat and Mass Transfer in the Turbulent Flow in Pipes and Channels," NASA STI/Recon Tech. Rep. A, **41**(1), pp. 8–16.
- [25] Dunn, P. F., 2014, *Measurement and Data Analysis for Engineering and Science*, CRC Press, Boca Raton, FL.
- [26] Mazzei, L., Da Soghe, R., and Bianchini, C., 2020, "CFD Modelling Strategies for the Simulation of Roughness Effects on Friction and Heat Transfer in Additive Manufactured Components," ASME Turbo Expo 2020: Turbomachinery Technical Conference and Exposition, Virtual, Online, Paper No. GT2020-15406.
- [27] ANSYS, 2018, *Ansys Fluent*, ANSYS, Canonsburg, PA.
- [28] Kirsch, K. L., and Thole, K. A., 2018, "Isolating the Effects of Surface Roughness Versus Wall Shape in Numerically Optimized, Additively Manufactured Micro Cooling Channels," *Exp. Therm. Fluid. Sci.*, **98**, pp. 227–238.
- [29] Pointwise, 2018, *Pointwise*, Pointwise, Fort Worth, TX.
- [30] Gee, D. L., and Webb, R. L., 1980, "Forced Convection Heat Transfer in Helically Rib-Roughened Tubes," *Int. J. Heat Mass Transfer*, **23**(8), pp. 1127–1136.